

## SOLAR CELLS

# Interfacial toughening with self-assembled monolayers enhances perovskite solar cell reliability

Zhenghong Dai, Srinivas K. Yadavalli, Min Chen, Ali Abbaspourtamijani, Yue Qi, Nitin P. Padture\*

Iodine-terminated self-assembled monolayer (I-SAM) was used in perovskite solar cells (PSCs) to achieve a 50% increase of adhesion toughness at the interface between the electron transport layer (ETL) and the halide perovskite thin film to enhance mechanical reliability. Treatment with I-SAM also increased the power conversion efficiency from 20.2% to 21.4%, reduced hysteresis, and improved operational stability with a projected T80 (time to 80% initial efficiency retained) increasing from ~700 hours to 4000 hours under 1-sun illumination and with continuous maximum power point tracking. Operational stability-tested PSC without SAMs revealed extensive irreversible morphological degradation at the ETL/perovskite interface, including voids formation and delamination, whereas PSCs with I-SAM exhibited minimal damage accumulation. This difference was attributed to a combination of a decrease in hydroxyl groups at the interface and the higher interfacial toughness.

The promise of low cost, high power conversion efficiency (PCE), and versatility has driven research efforts on perovskite solar cells (PSCs) (1–3). The low formation energies of metal halide perovskite (MHP) light absorbers that enable solution processing at or near room temperature (4) also make them unstable (5, 6). Research on improving PSC operational stability (5, 6) together with scalability (7) has made steady progress, but PSCs will also need to be mechanically reliable if they are to operate efficiently for decades (6, 8–11). Enhancing the mechanical reliability of PSCs is particularly challenging because the low formation energies of MHPs result in inherently poor mechanical properties, meaning that they are compliant (low Young's modulus,  $E$ ), soft (low hardness,  $H$ ), and brittle (low toughness,  $G_C$ ) (9). For example, the prototypical MHP, methylammonium lead triiodide ( $\text{CH}_3\text{NH}_3\text{PbI}_3$ , or  $\text{MAPbI}_3$ ), has  $E \sim 17.8$  GPa,  $H \sim 0.6$  GPa, and  $G_C \sim 2.7$  J·m<sup>-2</sup> (cohesion), as measured by nanoindentation of single crystals (9). Furthermore, interfaces between the MHP thin film and the adjacent functional layers in the planar PSC multilayer stack are even more brittle, with  $G_C < 1.5$  J·m<sup>-2</sup> (adhesion) typically (8, 10, 12, 13), making them prone to premature delamination.

The sources of internal and external mechanical stresses in PSCs that can drive fracture include (9, 11) (i) coefficient of thermal expansion (CTE) mismatch between the layers; (ii) in-service thermal excursions; (iii) in-service damage accumulation; and (iv) deformation during manufacturing, installation, maintenance, and service (such as bending, stretching, and twisting). In tandem photovoltaics (PVs) incorporating PSCs, the CTE-induced internal stresses are expected to be even higher owing

to the additional layers, and in the case of flexible single-junction PSCs, the externally applied stresses are typically more severe (9, 11). Although the ultimate in-service delamination failure of devices depends on many factors,  $G_C$  of the weakest interface—akin to the weakest link in a chain—is perhaps the most important metric that determines the mechanical reliability of multilayer devices (14).

There have been a few attempts to enhance the  $G_C$  of the weakest interface in PSCs, with varying degrees of success, using approaches such as adding interfacial layers (10, 15–18), scaffolding (19), interpenetrating interfaces (20), introducing additives (13, 21), and grain coarsening (12). In this study, we demonstrate the substantial toughening of the brittle interface between the MHP thin film and the underlying  $\text{SnO}_2$  electron transport layer (ETL) using an iodine-terminated self-assembled monolayer (I-SAM) that acts as a “molecular glue.” This processing step not only increased PCE (up to 21.44%) and reduced hysteresis but also improved operational stability under 1-sun maximum power point (MPP) continuous operation [projected T80 (time to 80% initial PCE retained) up to ~4000 hours]. The characterization of the operational stability-tested PSCs reveals that the I-SAM helped preserve the mechanical integrity of the ETL/MHP interface, and what is called operational stability in previous PSC studies is closely intertwined with mechanical reliability. We note that SAMs have been used to toughen interfaces in other types of devices while improving other functional properties, for example, thermal conductivity (22).

We chose the mixed-composition MHP,  $\text{Cs}_{0.05}(\text{FA}_{0.85}\text{MA}_{0.15})_{0.95}\text{Pb}(\text{I}_{0.85}\text{Br}_{0.15})_3$  with 4 mol % excess  $\text{PbI}_2$  [FA = formamidinium or  $\text{HC}(\text{NH}_2)_2^+$ ], optimized for high PCE and stability (23) and  $\text{SnO}_2$  as the ETL, as it provides a more favorable energy-level alignment with this MHP and minimizes the photo-

catalytic degradation of the MHP compared with  $\text{TiO}_2$ . The 3-iodopropyl trimethoxysilane [ $\text{Si}(\text{OCH}_3)_3(\text{CH}_2)_3\text{I}$ ] I-SAM, with  $-\text{Si}(\text{OCH}_3)_3$  anchor group,  $-\text{I}$  terminal group, and alkyl  $(\text{CH}_2)_n$  chain ( $n = 3$ ) linker, was chosen on the basis of the following considerations. First, the surface of the  $\text{SnO}_2$  ETL, as in most oxides (24), is covered with adsorbed hydroxyl ( $-\text{OH}$ ) groups that get trapped during deposition of the MHP thin film on top in n-i-p “regular” planar PSCs and degrade performance (25, 26). Trialkoxysilane SAMs are known to self-assemble and cross-link readily on such oxide surfaces by the silanization process (27) and greatly reduce the number of surface  $-\text{OH}$  groups as they create anchoring O–Si bonds. Second, assuming a “brushlike” SAM morphology due to the short alkyl chain length used here, the  $-\text{I}$  terminal group is expected to form electrostatic bonds to the MHP thin film on top (28). A control H-SAM with a  $-\text{H}$  terminal group [ $\text{Si}(\text{OCH}_3)_3(\text{CH}_2)_3\text{H}$ ] was used in separate experiments to isolate the effects of the  $-\text{I}$  terminal group. Third, the short length of the alkyl chain ( $n = 3$ ) makes the SAM-coated surface sufficiently lyophilic for the subsequent solution deposition of the MHP thin film. Finally, SAMs in general (29, 30), and trialkoxysilane-based SAMs in particular (31, 32), increase PCE and reduce hysteresis in PSCs through improved extraction of photocarriers, reduced charge accumulation at interfaces, and passivation of interfacial charge traps.

We measured the adhesion toughness,  $G_C$ , of the ETL/MHP interface using the “sandwich” double-cantilever beam (DCB) delamination method (Fig. 1A) (8, 10, 12, 14), as described in the supplementary materials (SM) and fig. S1. The  $\text{SnO}_2$  ETL was deposited on indium tin oxide (ITO)-coated glass substrates using the method of Jiang *et al.* (33). The SAM was deposited on the  $\text{SnO}_2$  surface by dip-coating at room temperature using the procedure described in the SM. We note that SAM deposition is sensitive to several experimental parameters, including water content, solvent used, solution age, deposition time, temperature, etc. (27). The presence of Si on the H-SAM-coated ETL surface and both Si and I on the I-SAM-coated ETL surface was confirmed with x-ray photoelectron spectroscopy (XPS) (fig. S2). The MHP thin film (~500-nm thickness) was then deposited through a variation of the solvent-engineering method (34). X-ray diffraction (XRD) patterns of the MHP thin films without SAMs and ones with H-SAM or I-SAM underneath (fig. S3) showed no difference in the thin-film MHP phase. Similarly, the top-surface scanning electron microscopy (SEM) images in fig. S4 showed no discernible difference in the MHP thin-film microstructure; the average apparent grain sizes of the MHP thin films are between ~330 and ~370 nm.

School of Engineering, Brown University, Providence, RI 02912, USA.

\*Corresponding author. Email: nitin\_padture@brown.edu

The  $G_C$  of the ETL/MHP interface (Fig. 1B and table S1) was enhanced by ~50% with I-SAM ( $1.91 \pm 0.48$  to  $2.83 \pm 0.35$  J·m<sup>-2</sup>). For H-SAM, the mechanical bonding with MHP was weak, resulting in  $G_C$  decreasing to  $1.72 \pm 0.54$  J·m<sup>-2</sup>. Delamination failure occurred at the ETL/MHP interface in each case; SEM images of the mating fracture surfaces are shown in fig. S5. For the I-SAM case, the SEM image of the SnO<sub>2</sub> ETL side fracture surface showed a few adhered smaller MHP grains due to occasional intergranular fracture.

Density functional theory (DFT) calculations were performed to study the adhesion provided by the interfacial bonding between the MHP surface and idealized brushlike SAMs (see SM for details) (35–42), where we used  $\alpha$ -FAPbI<sub>3</sub> to represent the MHP. Aligned butane [H(CH<sub>2</sub>)<sub>4</sub>H] and I-terminated butane [(H(CH<sub>2</sub>)<sub>4</sub>I) molecules were used to represent H-SAM and I-SAM, respectively, because the Si-based anchor group in the SAMs was unlikely to influence the bonding at the other end of the alkyl chains. The adhesion of  $\alpha$ -FAPbI<sub>3</sub> (001) surfaces, of different terminations, with H(CH<sub>2</sub>)<sub>4</sub>I was found to be about twice that with H(CH<sub>2</sub>)<sub>4</sub>H (table S2 and fig. S6). The strongest adhesion was achieved at the PbI<sub>2</sub>-terminated  $\alpha$ -FAPbI<sub>3</sub> (001) surface with two aligned H(CH<sub>2</sub>)<sub>4</sub>I molecules per unit cell (near-ideal packing density of 20 Å<sup>2</sup> per molecule). The interfacial bonding with I-SAM has the characteristics of the halogen bond, where a low-electron density region on a covalently bonded halogen atom (mainly in the heavier halogens) forms attractive interaction with electron-rich sites (43). The electrophilic regions associated with the halogen atoms on H(CH<sub>2</sub>)<sub>4</sub>I gained electrons from both the undercoordinated Pb<sup>2+</sup> (electron donor) and fully coordinated I<sup>−</sup> (nucleophile) on the PbI<sub>2</sub>-terminated  $\alpha$ -FAPbI<sub>3</sub> (001) surface (Fig. 1D). Halogen bonding changes with electrophilic order: I > Br > Cl > F, which increases with polarizability and decreases with electronegativity. A similar interface using H(CH<sub>2</sub>)<sub>4</sub>F molecules at the other extreme of the electrophilic order confirms this trend (table S2). Naturally, no such bond is expected at the interface with H(CH<sub>2</sub>)<sub>4</sub>H (Fig. 1C). The lack of electron transfer and the longer I⋯H and Pb⋯H distances indicated the absence of chemical bonding (see fig. S6 and table S2 for other  $\alpha$ -FAPbI<sub>3</sub> surface terminations and different packing densities). Although I-SAM in the experiments may not be as idealized (i.e., brushlike, full-coverage), the DFT calculations support the hypothesis that I-termination enhances the bonding with the MHP surface substantially and that it is preferred over other halogen terminations. The latter was further confirmed experimentally using 3-bromopropyl trimethoxysilane [Si(OCH<sub>3</sub>)<sub>3</sub>(CH<sub>2</sub>)<sub>3</sub>Br] Br-SAM, where an average  $G_r$  of

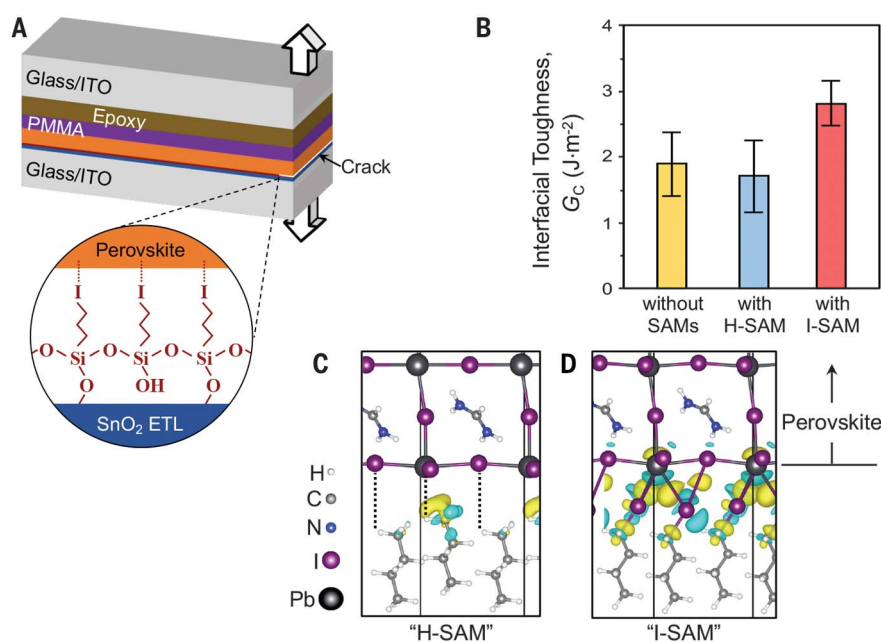


**Fig. 1. Mechanical behavior of the ETL/MHP interface.** (A) Schematic illustration of the sandwich DCB specimen for toughness testing (not to scale). PMMA, poly(methyl methacrylate). Inset shows magnified schematic illustration of idealized I-SAM. (B) Toughness of ETL/MHP interface without SAMs and ones with H-SAM or I-SAM. The histograms and error bars represent average and standard deviation, respectively, of 12 specimens each (see table S1 for the data). (C and D) Charge transfer density difference plots from DFT calculations. Bonding between  $\text{PbI}_2$ -terminated  $\alpha$ -FAPbI<sub>3</sub> (001) surface and (C)  $\text{H}(\text{CH}_2)_3\text{H}$  ("H-SAM") or (D)  $\text{H}(\text{CH}_2)_3\text{I}$  ("I-SAM"). The yellow and blue colors indicate electron gain or loss above  $0.0047 \text{ e}^- \text{\AA}^{-3}$ , respectively. Dashed lines across the interface indicate no bonding.

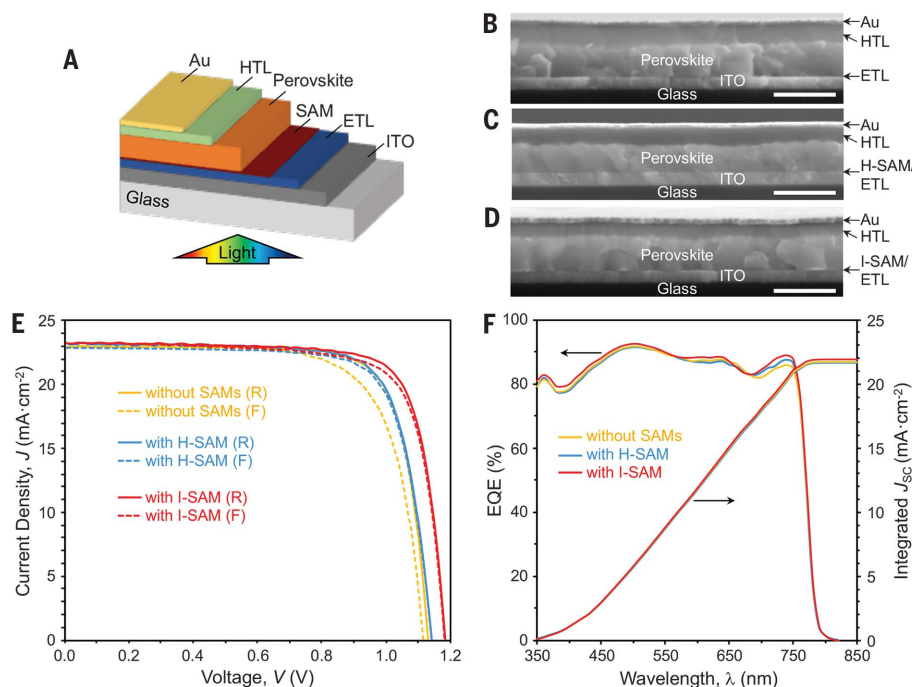


**Fig. 2. Structure and performance of PSCs.** (A) Schematic illustration (not to scale) of the n-i-p regular planar PSCs with SAMs (SAMs absent in control PSC). HTL, hole transport layer. Cross-sectional SEM images of as-fabricated PSCs: (B) without SAMs, (C) with H-SAM, and (D) with I-SAM. Scale bars, 1  $\mu\text{m}$ . (E) J-V responses, in reverse (R) and forward (F) scans, of champion PSCs without SAMs and ones with H-SAM or I-SAM. (See Table 1 for PV performance parameters.) (F) EQE spectra and integrated  $J_{\text{SC}}$  of the champion PSCs without SAMs and ones with H-SAM or I-SAM.

**Fig. 3. Operational stability of PSCs.** Normalized PCE of PSCs without SAMs and ones with H-SAM or I-SAM (three devices) as a function of time under the following conditions: 1-sun continuous illumination, MPP tracking, unencapsulated, flowing N<sub>2</sub> atmosphere, and room temperature. PCE was recorded about every hour. The lines are linear fits to the data after initial burn-in and nonmonotonic behavior, where the y intercept and the slope are used to estimate and project the T80 duration.

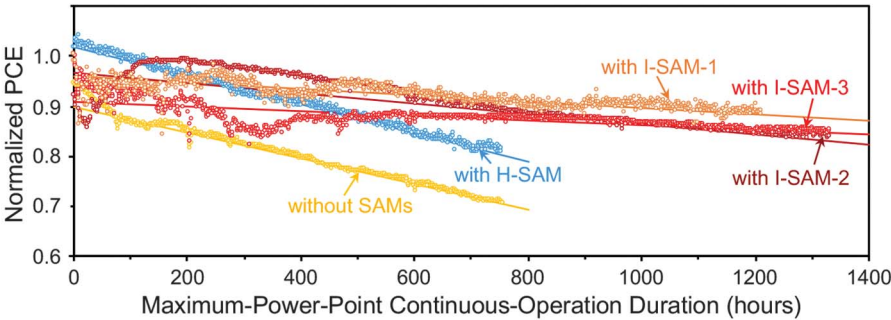


Table 1. PV performance parameters. Values extracted from the J-V data, in reverse (R) and forward (F) scans, of champion PSCs without SAMs and ones with H-SAM or I-SAM.					
PSC	Scan	V <sub>OC</sub> (V)	J <sub>SC</sub> (mA·cm <sup>-2</sup> )	FF	PCE (%)
Without SAMs	R	1.131	23.02	0.774	20.15
	F	1.117	22.99	0.721	18.52
With H-SAM	R	1.143	23.18	0.762	20.19
	F	1.142	22.86	0.760	19.84
With I-SAM	R	1.185	23.26	0.778	21.44
	F	1.182	23.22	0.759	20.83

2.08 ± 0.31 J·m<sup>-2</sup> was measured (table S1), which falls in between the H-SAM and I-SAM cases.

We fabricated PSCs with planar n-i-p regular architecture (Fig. 2A) for different SAMs (see SM for device fabrication and testing details). Cross-sectional SEM images in Fig. 2, B to D, showed no discernible differences. The current density (*J*)-voltage (*V*) response of the “champion” (i.e., best-performing) PSCs without SAMs and the ones with H-SAM or I-SAM are presented in Fig. 2E, and the corresponding PV performance parameters are listed in Table 1. The I-SAM increased open-circuit voltage (*V*<sub>OC</sub>), and both PSCs with SAMs showed lower hysteresis indices (1.8% H-SAM and 2.9% I-SAM versus 8.8% without SAMs). The short-circuit current density (*J*<sub>SC</sub>) values for all PSCs compared favorably with the respective values derived from the external quantum efficiency (EQE) spectra of these PSCs in Fig. 2F. The stabilized PCE output at MPP of these three PSCs is presented in fig. S7.

Statistics for the PV performance parameters *J*<sub>SC</sub>, *V*<sub>OC</sub>, fill factor (FF), and PCE for PSCs (20 of each type) are presented in fig. S8, with an average PCE of 19.04 ± 0.49% for PSCs without SAMs, 19.04 ± 0.48% for PSCs with H-SAM, and 20.20 ± 0.62% for PSCs with I-SAM, confirming overall increased performance of the latter and also demonstrating reproducibility. The increased PCE in PSCs with I-SAM was largely the result of the increased *V*<sub>OC</sub>. In this context, the estimated trap filled limit voltages (*V*<sub>TFL</sub>) for electron-only transport devices

shown in fig. S9 were used to estimate trap densities (*n*<sub>trap</sub>) of 5.21 × 10<sup>15</sup> cm<sup>-3</sup> for the device without SAMs, 1.98 × 10<sup>15</sup> cm<sup>-3</sup> for the device with H-SAM, 1.36 × 10<sup>15</sup> cm<sup>-3</sup> for the device with I-SAM. We attributed the increased *V*<sub>OC</sub> to the passivation of charge traps by I-SAM that improved extraction of electrons. The reduced hysteresis with both SAMs was attributed to the reduced charge accumulation with fewer surface -OH groups. Similar increases in PSC performance with different types of SAMs have been demonstrated in several studies (25, 28–32).

In Fig. 3, we present the operational stability of PSCs under continuous 1-sun illumination with MPP tracking. In all the tested PSCs, there was initial burn-in instability with a decline, rise, or both in PCE followed by linear steady-state degradation, as has been seen previously for single-junction PSCs (44). Following a method proposed by Khenkin *et al.* (44), we estimated a T80 of ~692 hours for PSCs without SAMs and ~714 hours for PSCs with H-SAM (see SM for details). The steady-state degradation of these PSCs appeared to occur at about the same rate. The extrapolated T80 durations for the three PSCs with I-SAM, assuming linear degradation, were estimated at ~3006, ~1896, and ~3921 hours. The normalized PV performance parameters (*J*<sub>SC</sub>, *V*<sub>OC</sub>, FF, and PCE) of the PSCs from the *J-V* responses measured during operational stability testing are presented in fig. S10. [Note that PCE derived from the *J-V* response was typically higher than that measured by MPP tracking (44, 45).] The performance degradation in the PSC without SAMs

was in all three parameters, *J*<sub>SC</sub>, *V*<sub>OC</sub>, and FF. Table S3 presents PV performance parameters of the PSCs with SAMs, before and after the completion of operational stability testing, showing decay primarily in *V*<sub>OC</sub> and FF.

The operational stability-tested PSCs were characterized by cross-sectioning one half of each of these devices and deliberately delaminating the other half. Cross-sectional SEM images of the PSC without SAMs (Fig. 4, A to C) showed three types of irreversible morphological degradation features at the interface compared with the corresponding “before” SEM image in Fig. 2B: small voids, large voids, and delamination. In the PSC with H-SAM (Fig. 4D), although voids were not apparent, interfacial delamination was observed. In contrast, such degradation features were not seen in the PSC with I-SAM in the SEM image in Fig. 4E, which looked similar to the corresponding “before” SEM image in Fig. 2D.

Figure 4, F to I, shows SEM images of the perovskite bottom side fracture surfaces of the same delaminated PSCs. Consistent with the cross-sectional observations, the perovskite bottom side fracture surface of the PSC without SAMs showed small voids, large voids (Fig. 4F), and delamination (Fig. 4G). Light-contrast degradation-product particles were also seen in Fig. 4, F and G, which were absent in the pristine interface (fig. S5B). In the PSC with H-SAM (Fig. 4H), delamination and some voids were observed. In comparison, degradation features in the PSCs with I-SAM were relatively unremarkable (Fig. 4I), which is,



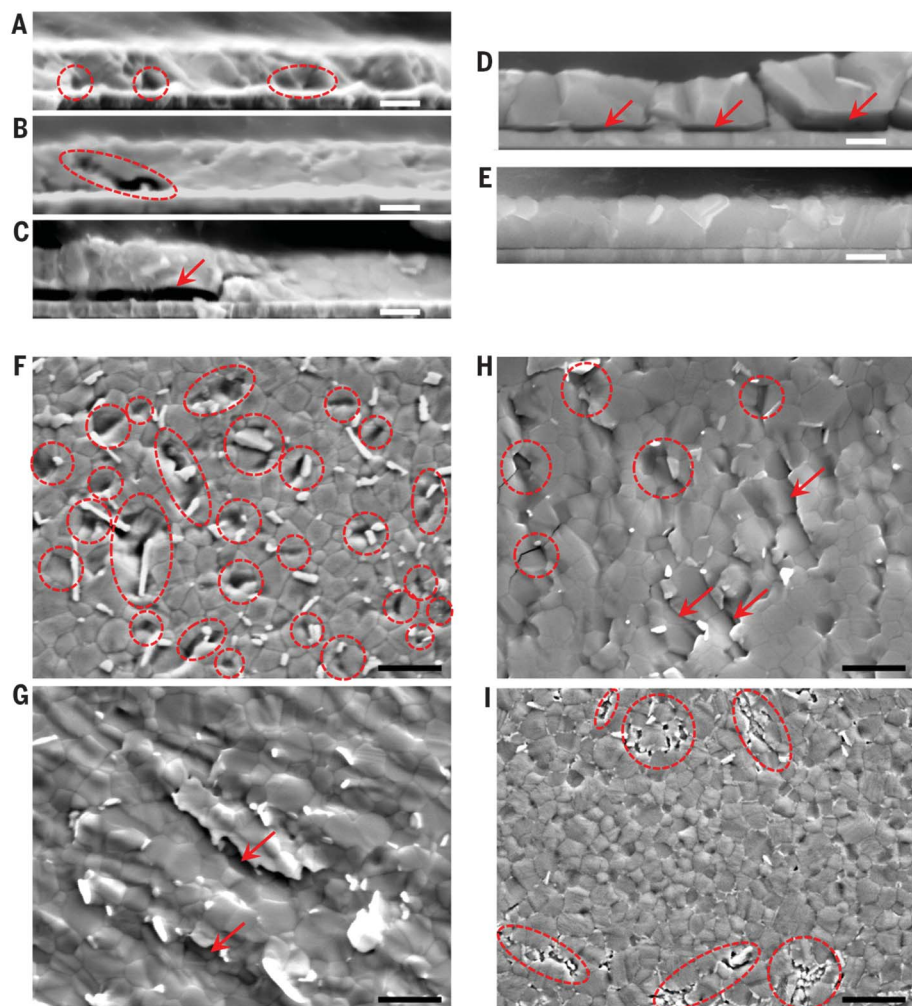


**Fig. 4. Characterization of operational stability-tested PSCs.** (A to C) Cross-sectional SEM images of the PSC without SAMs tested for 757 hours showing morphological degradation at the ETL/MHP interface: (A) small voids (dashed circles/ovals), (B) large voids (dashed oval), and (C) delamination (arrow). (D) Cross-sectional SEM image of the PSC with H-SAM tested for 754 hours showing delamination (arrows). (E) Cross-sectional SEM image of a PSC with I-SAM tested for 1331 hours with intact ETL/MHP interface. (F and G) SEM images of fracture surface (perovskite bottom side) of the PSC without SAMs showing: (F) small and large voids (dashed circles/ovals) and (G) interfacial delamination (arrows). (H) Corresponding SEM image of the PSC with H-SAM showing voids (dashed circles/ovals) and delamination (arrows). (I) Corresponding SEM image of the PSC with I-SAM showing minimal morphological degradation (dashed circles/ovals). Scale bars, 0.5  $\mu\text{m}$  [(A) to (E)] and 1  $\mu\text{m}$  [(F) to (I)].

once again, consistent with the corresponding cross-sectional SEM image (Fig. 4E).

We attributed the reduced severity of irreversible degradation of the ETL/MHP interface with I-SAM, and the attendant decay in the PSC performance, to the following effects of the I-SAM. First, both H-SAM and I-SAM should reduce the prevalence of  $-\text{OH}$  groups at the  $\text{SnO}_2$  ETL surface. This results in the reduction of the concentration of positively charged point defects (25), which should slow down the ion migration-induced formation of interfacial voids that can serve as sites for photocarrier recombination (46) and nucleation of interfacial delamination cracks. The enhanced  $G_C$  of the ETL/MHP interface with

I-SAM should impede propagation of these incipient interfacial delamination cracks that would block electric current (46). To isolate the effect of light, we exposed the DCB specimens without SAMs and the ones with H-SAM or I-SAM to 1-sun (light-emitting diode) continuous illumination in air ( $\sim 35^\circ\text{C}$ ,  $\sim 40\%$  relative humidity) from the bottom for 120 or 240 hours and then tested them to measure the  $G_C$ . The results in fig. S11 and table S4 show that after 240-hour exposure there was 14 and 17% loss in the average  $G_C$  in PSCs without SAMs and those with H-SAM, respectively, but only 5% for those with I-SAM. This suggested that the light-induced reduction in  $G_C$  in specimens without SAMs and

ones with H-SAM, both with initial lower  $G_C$  (Fig. 1B), also contributed to the degradation of their respective PSCs.

We chose the most brittle interface (ETL/MHP) in PSCs for SAM-induced toughening for maximum impact. When sufficiently toughened, delamination failure will shift to the next weakest interface in the PSC multilayer stack, and so on (9, 10), so future efforts will need to focus on toughening the other PSC interfaces using SAMs. Room-temperature solution deposition of SAMs is a low-cost approach that is amenable to scale-up for batch and/or continuous manufacturing of a wide variety of PSCs (rigid, flexible, and tandem). Eventually, when all the interfaces are sufficiently toughened and optimized, the ultimate failure of PSCs will be determined by fracture within the individual layers. Toughening of the individual layers themselves, for example, by incorporating reinforcements as in ceramic or polymer nanocomposites, while simultaneously improving their functional properties, will be the next challenge.

## REFERENCES AND NOTES

1. N.-G. Park, M. Grätzel, T. Miyasaka, *Organic-Inorganic Halide Perovskite Photovoltaics: From Fundamentals to Device Architectures* (Springer, 2016).
2. H. J. Snaith, *Nat. Mater.* **17**, 372–376 (2018).
3. A. K. Jena, A. Kulkarni, T. Miyasaka, *Chem. Rev.* **119**, 3036–3103 (2019).
4. W. A. Dunlap-Shohl, Y. Zhou, N. P. Padture, D. B. Mitzi, *Chem. Rev.* **119**, 3193–3295 (2019).
5. Y. Rong et al., *Science* **361**, eaat8235 (2018).
6. S. P. Dunfield et al., *Adv. Energy Mater.* **10**, 1904054 (2020).
7. Z. Li et al., *Nat. Rev. Mater.* **3**, 18017 (2018).
8. N. Rolston et al., *Extreme Mech. Lett.* **9**, 353–358 (2016).
9. C. Ramirez, S. K. Yadavalli, H. F. Garces, Y. Zhou, N. P. Padture, *Scr. Mater.* **150**, 36–41 (2018).
10. N. Rolston et al., *Adv. Energy Mater.* **8**, 1702116 (2018).
11. S. K. Yadavalli, Z. Dai, H. Zhou, Y. Zhou, N. P. Padture, *Acta Mater.* **187**, 112–121 (2020).
12. Z. Dai et al., *Scr. Mater.* **185**, 47–50 (2020).
13. M. Gutwald et al., *Sol. Energy Mater. Sol. Cells* **209**, 110433 (2020).
14. J.-H. Kim et al., *MRS Bull.* **42**, 115–123 (2017).
15. J. H. Yun et al., *J. Mater. Chem. A* **3**, 22176–22182 (2015).
16. B. L. Watson et al., *ACS Appl. Mater. Interfaces* **8**, 25896–25904 (2016).
17. S. Jeong, I. Lee, T.-S. Kim, J.-Y. Lee, *Adv. Mater. Interfaces* **7**, 2001425 (2020).
18. S. Song et al., *Adv. Energy Mater.* **11**, 2003382 (2021).
19. B. L. Watson, N. Rolston, A. D. Printz, R. H. Dauskardt, *Energy Environ. Sci.* **10**, 2500–2508 (2017).
20. Q. Dong et al., *Nat. Commun.* **12**, 973 (2021).
21. J. Tong et al., *Matter* **4**, 1365–1376 (2021).
22. P. J. O'Brien et al., *Nat. Mater.* **12**, 118–122 (2013).
23. M. Saliba et al., *Energy Environ. Sci.* **9**, 1989–1997 (2016).
24. C. Noguera, *Physics and Chemistry at Oxide Surfaces* (Cambridge Univ. Press, 1996).
25. G. Tumen-Ulzii et al., *Commun. Mater.* **1**, 31 (2020).
26. Z. Liu et al., *Nat. Energy* **5**, 596–604 (2020).
27. A. Ulman, *Chem. Rev.* **96**, 1533–1554 (1996).
28. A. Abate et al., *Nano Lett.* **14**, 3247–3254 (2014).
29. P. Schulz, D. Cahen, A. Kahn, *Chem. Rev.* **119**, 3349–3417 (2019).
30. S. Y. Kim, S. J. Cho, S. E. Byeon, X. He, H. Y. Yoon, *Adv. Energy Mater.* **10**, 2002606 (2020).
31. L. Liu et al., *J. Am. Chem. Soc.* **137**, 1790–1793 (2015).
32. G. Yang et al., *J. Mater. Chem. A* **5**, 1658–1666 (2017).
33. Q. Jiang et al., *Nat. Energy* **2**, 16177 (2017).
34. N. J. Jeon et al., *Nat. Mater.* **13**, 897–903 (2014).
35. G. Kresse, J. Furthmüller, *Comput. Mater. Sci.* **6**, 15–50 (1996).
36. G. Kresse, J. Furthmüller, *Phys. Rev. B* **54**, 11169–11186 (1996).

37. J. P. Perdew, K. Burke, M. Ernzerhof, *Phys. Rev. Lett.* **77**, 3865–3868 (1996).
38. S. Grimme, J. Antony, S. Ehrlich, H. Krieg, *J. Chem. Phys.* **132**, 154104 (2010).
39. A. A. Tamijani, A. Salam, M. P. de Lara-Castells, *J. Phys. Chem. C* **120**, 18126–18139 (2016).
40. M. T. Weller, O. J. Weber, J. M. Frost, A. Walsh, *J. Phys. Chem. Lett.* **6**, 3209–3212 (2015).
41. J. Liu *et al.*, *Phys. Chem. Chem. Phys.* **22**, 19718–19724 (2020).
42. Y. Qi, L. G. Hector, *Phys. Rev. B* **69**, 235401 (2004).
43. G. Cavallo *et al.*, *Chem. Rev.* **116**, 2478–2601 (2016).
44. M. V. Khenkin *et al.*, *Nat. Energy* **5**, 35–49 (2020).
45. M. Saliba, M. Stollerfoht, C. M. Wolff, D. Neher, A. Abate, *Joule* **2**, 1019–1027 (2018).
46. D. Bi *et al.*, *Nat. Commun.* **9**, 4482 (2018).

## ACKNOWLEDGMENTS

Experimental assistance from M. Hu, N. Pellet, and Y. Zhou is gratefully acknowledged. **Funding:** The work of Z.D., S.K.Y., M.C., and N.P.P. was supported by the Office of Naval Research (grants N00014-17-1-2232 and N00014-20-1-2574) and the National Science Foundation (NSF; grant 1538893). The work of A.A. and Y.Q. was supported by NSF Center for Synthetic Organic Electrochemistry (grant 2002158). **Author contributions:** N.P.P. conceived of, designed, and supervised the research. Z.D., S.K.Y., and M.C. fabricated the thin films and the devices. Z.D. characterized and tested the thin films and the devices. A.A. and Y.Q. performed the DFT calculations. N.P.P. and Z.D. interpreted the data and wrote the manuscript, with contributions from the other authors. **Competing interests:** The authors declare no competing interests.

Provisional application for a patent has been filed. **Data and materials availability:** All data are available in the main text or the supplementary materials.

## SUPPLEMENTARY MATERIALS

science.sciencemag.org/content/372/6542/618/suppl/DC1  
Materials and Methods  
Supplementary Text  
Figs. S1 to S11  
Tables S1 to S4  
References

20 November 2020; resubmitted 25 February 2021  
Accepted 6 April 2021  
10.1126/science.abf5602

## Interfacial toughening with self-assembled monolayers enhances perovskite solar cell reliability

Zhenghong DaiSrinivas K. YadavalliMin ChenAli AbbaspourtamijaniYue QiNitin P. Padture

*Science*, 372 (6542), • DOI: 10.1126/science.abf5602

### Tougher solar cell interfaces

The low formation energies of the active layers in perovskite solar cells lead to low-toughness materials that are compliant and soft, which limits their interface stability and long-term reliability. Dai *et al.* show that treatment with iodine-terminated self-assembled monolayers that react with surface hydroxyl groups (which ultimately creates unwanted charge traps and voids) leads to a 50% increase of adhesion toughness between the electron transport layer and a mixed-composition perovskite thin film. The projected point at which 80% of the operating efficiency in perovskite solar cells was still retained increased from #700 to 4000 hours for 1-sun exposure with continuous maximum power point tracking.

*Science*, this issue p. 618

### View the article online

<https://www.science.org/doi/10.1126/science.abf5602>

### Permissions

<https://www.science.org/help/reprints-and-permissions>

Use of this article is subject to the [Terms of service](#)